ADVANCED FUNCTIONAL MATERIALS
www.afm-journal.de

Thermally Conductive Hexagonal Boron Nitride/Polymer Composites for Efficient Heat Transport

*Chengning Yao, Grigore Leahu, Martin Holicky, Sihui Liu, Benji Fenech-Salerno, May Ching Lai, Maria Cristina Larciprete, Caterina Ducati, Giorgio Divitini, Roberto Li Voti, Concita Sibilia, and Felice Torrisi**

Commercial thermally conductive dielectric materials used in electronic packaging typically exhibit thermal conductivities (κ) ranging from 0.8 to 4.2 W m^{-1} K^{-1}. Hexagonal boron nitride (h-BN) flakes are promising thermally conductive materials for the thermal management of next-generation electronics. These electrically insulating yet thermally conducting h-BN flakes can be incorporated as thermal fillers to impart high κ to polymer-based composites. A cellulose-based composite embedded with few-layer h-BN (FLh-BN) flakes, achieving a $\kappa \approx 21.7$ W m^{-1} K^{-1}, prepared using a cost-effective and scalable procedure is demonstrated. This value is >5 times higher than the κ observed in composites embedded with bulk h-BN (Bh-BN, $\kappa \approx 4.5$ W m^{-1} K^{-1}), indicating the benefits of the superior κ of FLh-BN on the κ of h-BN polymer composites. When applied as a paste for thermal interface material (TIM), the FLh-BN composite can reduce the maximum temperature (T_{max}) by 24.5 °C of a heating pad at a power density (h) of 2.48 W cm^{-2} compared to Bh-BN composites at the same h-BN loading. The results provide an effective approach to improve the κ of cellulose-based thermal pastes for TIMs and demonstrate their viability for heat dissipation in integrated circuits (ICs) and high-power electronic devices.

1. Introduction

The continuous miniaturization of electronic devices and the ever-increasing device density in integrated circuits (IC)[1] results in a rapid increase in power density being generated in electronic chips. As a result, IC-relying devices such as power systems,[2,3] illuminated signs and displays,[4] switches, relays, inverters, and power supplies[1,5] will suffer from an ever-increasing local heating being generated by the embedded ICs. High power density peaks in a single device require efficient management of the generated heat (mainly by the Joule effect) during device operation, as they increase the device temperature, which can have detrimental effects on their performance, accelerating their failure rate and reducing their lifetime.[1] For these reasons, efficient and improved heat management systems will be crucial to ensure the reliable operation of electronic devices within an optimal operating temperature range.[6]

Typical thermal management systems mainly rely on two elements: first, a thermally conducting component (e.g., heat pipes[3] or thermal interface materials[7] (TIMs) to transport the heat away from hot spots via conduction, and second a heat sink/exchanger to dissipate the heat away into the environment (or a secondary fluid).[8] TIMs are frequently used in electronics, to reduce the thermal contact resistance between two surfaces and conduct heat efficiently.[9,10] TIMs are normally designed to be electrically insulating, thermally conducting,[11] easy to process on a large scale, and with a good thermal conductivity, κ (in the order or

C. Yao, M. Holicky, S. Liu, B. Fenech-Salerno, F. Torrisi
Department of Chemistry and Centre for Processable Electronics
Imperial College London
Molecular Sciences Research Hub
White City Campus, 82 Wood Lane, London W12 0BZ, UK
E-mail: f.torrisi@imperial.ac.uk

G. Leahu, M. C. Larciprete, R. L. Voti, C. Sibilia
Dipartimento di Scienze di Base ed Applicate per l'Ingegneria
Sapienza Università di Roma
Via A. Scarpa 16, Roma 00161, Italy

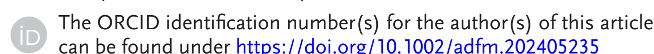
The ORCID identification number(s) for the author(s) of this article can be found under https://doi.org/10.1002/adfm.202405235

© 2024 The Author(s). Advanced Functional Materials published by Wiley-VCH GmbH. This is an open access article under the terms of the Creative Commons Attribution License, which permits use, distribution and reproduction in any medium, provided the original work is properly cited.

DOI: 10.1002/adfm.202405235

M. C. Lai, C. Ducati
Department of Materials Science and Metallurgy
27 Charles Babbage Road, Cambridge CB3 0FS, UK

G. Divitini
Electron Spectroscopy and Nanoscopy
Istituto Italiano di Tecnologia
Genova 16163, Italy

F. Torrisi
Dipartimento di Fisica e Astronomia
Università di Catania & CNR-IMM (Catania Universita')
Via S. Sofia 64, Catania 95123, Italy

one-order magnitude >1 W m^{-1} K^{-1}) and good surface wetting characteristics.[12]

Functional polymers (such as epoxy resins or polyvinyl alcohol) have become a popular candidate for preparing TIMs,[12–14] due to their excellent insulation, mechanical properties, and low processing costs. However, their practical use is limited due to a low κ value of ≈0.2 W m^{-1} K^{-1}.[15] To increase their κ, inorganic fillers with high κ are generally embedded with those functional polymers. For example, electrically conducting fillers like graphene and AgNW have improved the κ of polymers like epoxy, natural rubber, and polycarbonate,[7,16–18] but they pose an additional risk of short-circuits in electronic applications due to their electrically conducting nature. Electrically-insulating yet thermally conducting fillers are ideal for TIMs in electronics and electrical packaging, including oxides, such as Al_2O_3, SiO_2, and ZnO,[19–21] carbides such as SiC[22,23] and nitrides, such as AlN, BN, and Si_3N_4,[24,25] yielding commercial TIMs with $\kappa \approx 0.8$ – 4.2 W m^{-1} K^{-1}.[17,26] However, effective heat conduction and heat dissipation in miniaturized electronics with high power density require TIMs with $\kappa > 10$ W m^{-1} K^{-1}.[7,27,28,29]

Hexagonal boron nitride (h-BN) is a wide bandgap semiconducting layered material. Within each layer, alternating boron and nitrogen atoms are held together by sp^2 covalent bonds arranged on a honeycomb lattice, similar to graphene.[30] Monolayer h-BN (Mh-BN) shows intrinsic thermally conducting properties, with a theoretical in-plane κ calculated to reach ≈2000 W m^{-1} K^{-1}.[31,32] The in-plane κ in bulk h-BN (Bh-BN) was experimentally determined to be ≈370 W m^{-1} K^{-1},[30,33] and the κ increases with reduced thickness due to the reduction of interlayer phonon scattering.[33,34] The Bh-BN can be exfoliated into Mh-BN and few layer h-BN (FLh-BN) flakes, with a Mh-BN exhibiting a good anisotropy with an in-plane $\kappa \approx 751$ W m^{-1} K^{-1}[34] and an out-of-plane $\kappa \approx 5.2$ W m^{-1} K^{-1}.[35] However, currently commercial TIM products using h-BN as a thermal filler only report a $\kappa < 3$ W m^{-1} K^{-1}.[36–38]

Recent research studies have shown an improvement of κ in TIMs using h-BN as a thermal filler.[12] Zhao et al.[39] reported an epoxy/h-BN composite as a TIM for electronic packaging, reaching $\kappa \approx 1.09$ W m^{-1} K^{-1} at 40 wt.% of h-BN loading (while $\kappa \approx$ 0.2 W m^{-1} K^{-1} was measured with no h-BN loading). Xu et al.[40] also reported an epoxy-based composite but embedded with a 3D boron nitride foam (3D-BN), and the composite exhibits a $\kappa \approx$ 6.1 W m^{-1} K^{-1} at a 60 vol.% loading of 3D-BN. The κ value could be further improved by introducing well-aligned FLh-BN flakes in composites. For example, Kim et al.[41] reported that using an external magnetic field to align the FLh-BN in an epoxy composite can achieve a $\kappa \approx 3.445$ W m^{-1} K^{-1} (at 30 vol.% loading of FLh-BN), which was greatly improved compared to the composite without FLh-BN alignment ($\kappa \approx 1.765$ W m^{-1} K^{-1}). Han et al.[42] also proposed that using a freeze-drying treatment and subsequent infiltration can align the FLh-BN, and their epoxy/FLh-BN composite exhibited a $\kappa \approx 6.07$ W m^{-1} K^{-1} at 15 vol.% loading of FLh-BN. The choice of the polymer matrix plays a role in the κ values of as-prepared composites. For example, a poly-vinyl alcohol-based composite with 70 wt.% loading of aligned FLh-BN achieved a $\kappa \approx 24.6$ W m^{-1} K^{-1} using vacuum filtration,[43] and a PE-based composite reported in ref. [44] reached a $\kappa \approx 106.2$ W m^{-1} K^{-1} at a 15 wt.% loading of aligned BN nanoplatelets using a tensile force.

Cellulose is gaining more relevance as a polymer matrix for TIMs, as it can directly stabilize h-BN flakes in dispersions.[45] It is considered the most naturally abundant, eco-friendly, and biodegradable polymer, and is promising for the next generation of green electronics.[46] In addition, cellulose shows a higher Young's modulus (≈ 137.0 GPa) and a lower coefficient of thermal expansion (CTE < 10 ppm K^{-1})[47,48] than conventional polymers, such as epoxy with Young's modulus of ≈3.4 GPa[49] and CTE ≈45.8 ppm K^{-1}.[50,51] These advantages of cellulose make it a prime choice as a polymer matrix for thermally conducting composites and textiles.[52] Zeng et al.[53] prepared a BN-nanotube/cellulose film by vacuum filtration and the film shows an in-plane $\kappa \approx 21.4$ W m^{-1} K^{-1} at 25 wt.% loading of BN nanotube, while Tian et al.[54] functionalized the FLh-BN flakes with glycine to form a cellulose-based composite film, achieving $\kappa \approx$ 16.2 W m^{-1} K^{-1} at a 70 wt.% loading of FLh-BN. However, these production processes are not scalable, requiring externally applied magnetic fields or techniques such as vacuum filtration or hot pressing/stretching, which are inappropriate and costly for electronic grade TIMs. Moreover, the above-mentioned studies produced TIMs in the form of films rather than pastes. Pastes instead are ideal as they can fill any microscopic gaps between the two surfaces, providing better surface contact, surface wetting, heat transfer, and higher commercial viability.[12]

In this work, we demonstrate a FLh-BN/cellulose thermally conducting composite in the form of a thermal paste, reaching a κ of up to ≈21.7 W m^{-1} K^{-1}, which is one order of magnitude higher than that of commercial thermal pastes. The paste shows rheological characteristics, such as the viscosity $\eta \approx 273.6$ Pa s at 1 rpm. The FLh-BN paste is developed using a biocompatible, scalable, and low-cost process, which utilizes a one-pot mixing step compatible with industrial production. Our results untap the potential for commercial applications of thermally conducting FLh-BN pastes, by demonstrating their advantages as TIMs for the heat dissipation from hot spots to heat sinks. The FLh-BN paste demonstrated clear advantage in real applications, compared to equivalent Bh-BN pastes, achieving a 40% reduction in the maximum temperature, T_{max} reached by a hot surface, and a 9 °C reduction in the T_{max} of an operating high-power LED chip.

2. Results and Discussion

2.1. Synthesis of Hexagonal Boron Nitride and Composites

We prepared two types of composites (**Figure 1**) in the form of pastes to demonstrate the effect of Bh-BN or FLh-BN as thermal fillers in a sodium carboxymethyl cellulose (CMC) polymer matrix – a Bh-BN embedded composite (Bh-BN/CMC) and an FLh-BN embedded composite (FLh-BN/CMC) (details in methods).

Figure 1a shows the sample preparation of Bh-BN/CMC. Bh-BN and CMC powders are mixed by 5-min vortex to produce a homogenous mixture. The powder mixture is compressed using a hydraulic press (15 tons, 30 min) and is then dissolved in water to form a paste. The paste is shaped into a rod (13 mm in diameter) to create a symmetrical structure for κ measurements.[55]

The sample preparation of FLh-BN/CMC is illustrated in Figure 1b. The FLh-BN suspension is produced via ultrasonication-assisted liquid phase exfoliation (LPE), involving probe sonication (3 h) of pristine Bh-BN flakes in a solvent

© 2024 The Author(s). Advanced Functional Materials published by Wiley-VCH GmbH

16163028, 0, Downloaded from https://onlinelibrary.wiley.com/doi/10.1002/adfm.202405235 by Cochraneltalia, Wiley Online Library on [14/07/2024]. See the Terms and Conditions (https://onlinelibrary.wiley.com/terms-and-conditions) on Wiley Online Library for rules of use; OA articles are governed by the applicable Creative Commons License

16163028, 0, Downloaded from https://onlinelibrary.wiley.com/doi/10.1002/adfm.202405235 by Cochraneltalia, Wiley Online Library on [14/07/2024]. See the Terms and Conditions (https://onlinelibrary.wiley.com/terms-and-conditions) on Wiley Online Library for rules of use; OA articles are governed by the applicable Creative Commons License

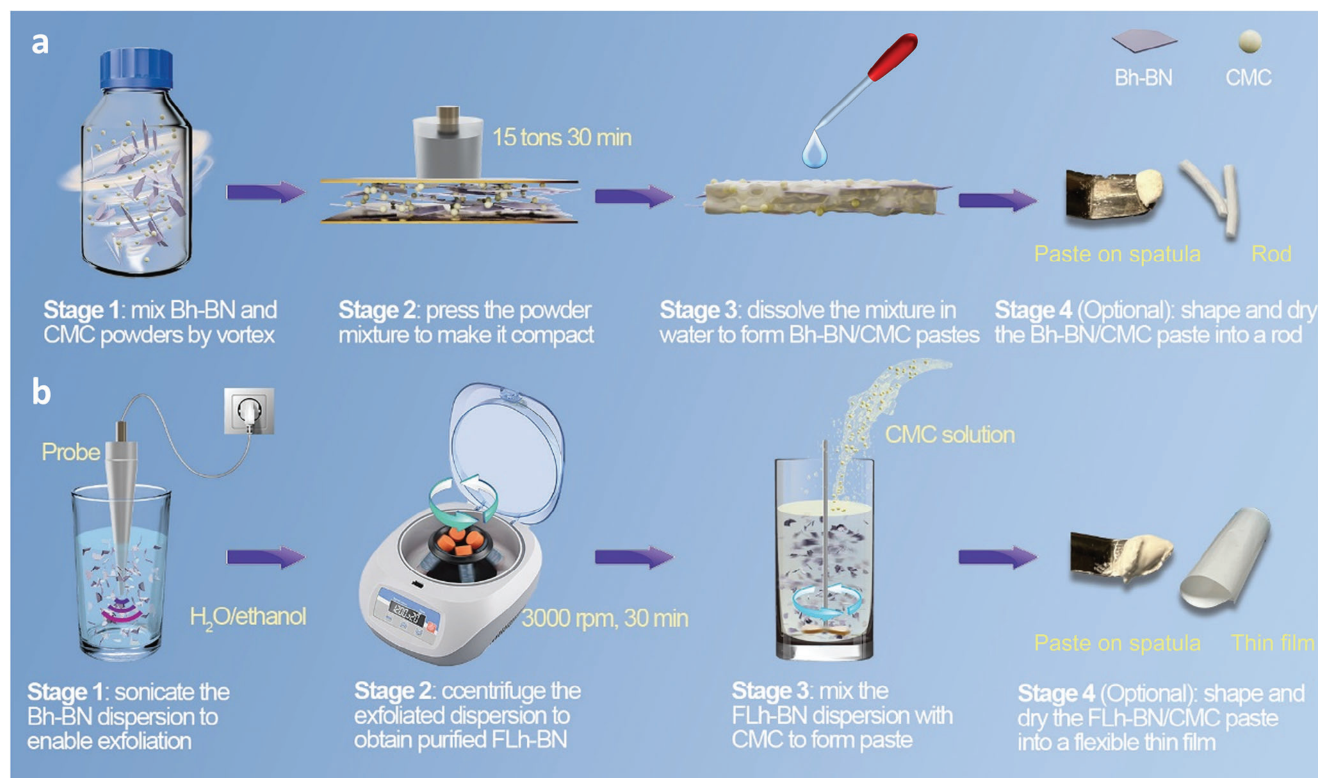

Figure 1. Schematic illustration of the sample preparation process of a) Bh-BN/CMC and b) FLh-BN/CMC, at room temperature.

mixture of water and ethanol,[56] followed by a centrifugation step (30 min, 3000 rpm) to remove any unexfoliated Bh-BN flakes.[45] After centrifugation, a 3 mg mL^{-1} CMC aqueous solution is mixed with the FLh-BN suspension and then stirred for 1 h to form a paste. The mixture is dried into a flexible thin film (≈7.5 μm thick) suitable for κ measurements.

The as-prepared pastes are composed of a homogeneous distribution of the Bh-BN or FLh-BN flakes (Figure S1.3, Supporting Information), as a result of the CMC acting as a stabilizer in the dispersion preventing the aggregation of the h-BN flakes.[57,58]

2.2. Characterization of Hexagonal Boron Nitride and Composites

Figure 2a shows the optical absorption spectrum of the FLh-BN suspension (shown in the inset). The spectrum shows a peak located at 205 nm, consistent with previous reports,[59,60] and corresponds to the inter-band transition in the density of states of h-BN, revealing an optical band gap at 6.04 eV. This value is consistent with previous results determining the optical band gap of the FLh-BN flakes from LPE.[45,60] Using the Beer-Lambert law $A = \alpha c l$, where A is the absorbance, l (m) is the beam path length, c (g L^{-1}) is the concentration, and α (L g^{-1} m^{-1}) is the absorption coefficient, we estimated a concentration of the FLh-BN flakes ($c_{\text{FLh-BN}}$)[61,62] in the suspension of $c_{\text{FLh-BN}} \approx 3.18$ mg mL^{-1}.

We used Raman spectroscopy (Figure 2b) and X-ray photoelectron spectroscopy (XPS) (Figure 2c,d; Figure S1a–c, Supporting Information) to monitor the quality of the materials. A single resonant Raman peak is observed for both Bh-BN and FLh-BN samples at 1366 and 1364 cm^{-1}, respectively, corresponding to the E_{2g} phonon vibrational mode. The downshifting of the peak in the case of the FLh-BN indicates the successful exfoliation of the Bh-BN into the FLh-BN flakes.[45,60,63] Figure 2c,d shows the XPS spectrum of the B1s and N1s regions of the FLh-BN flakes. The XPS peak centered at 190.4 eV in Figure 2c is formed due to the B—N bond within the FLh-BN structure,[64,65] and the peak centered at 398.0 eV in Figure 2d can be assigned to the binding energy of N—B bond,[66] in line with values reported in literature[64,67] for both peaks.

Figure 2e,f shows the atomic force microscopy (AFM) statistical analysis (acquired over 38 individual flakes) of the flake thickness (<t>) and the lateral flake size (<S>) of the FLh-BN. The statistic of <t> in Figure 2e follows a log-normal distribution, peaked at 6.1 nm. Assuming an interlayer distance of 3.35 Å[68,69] and an ≈1 nm water layer between the flake and the Si/SiO_2 substrate,[70,71] the FLh-BN suspension consists of a mean number of layers, $N \approx 15$. A statistic of $<S> = (xy)^{0.5}$ in Figure 2f, where x and y are the length and width of a FLh-BN flake, also follows a log-normal distribution, peaked at 339.0 nm. The mean aspect ratio (<S>/<t>) is calculated at 55.6. Figure 2g shows an AFM image of a FLh-BN flake on a Si/SiO_2 substrate with an <S> ≈ 210 nm, and a <t> ≈ 1.5 nm (height profile in Figure 2h), indicating a monolayer h-BN flake plus ≈ 1-nm water layer under the flake. This results in a large aspect ratio of 140. Scanning electron microscopy (SEM) was used to corroborate the statistical analysis of <S>. Figure 2i shows a typical scanning electron microscopy (SEM) image of the FLh-BN flakes deposited on a Si/SiO_2

 © 2024 The Author(s). Advanced Functional Materials published by Wiley-VCH GmbH

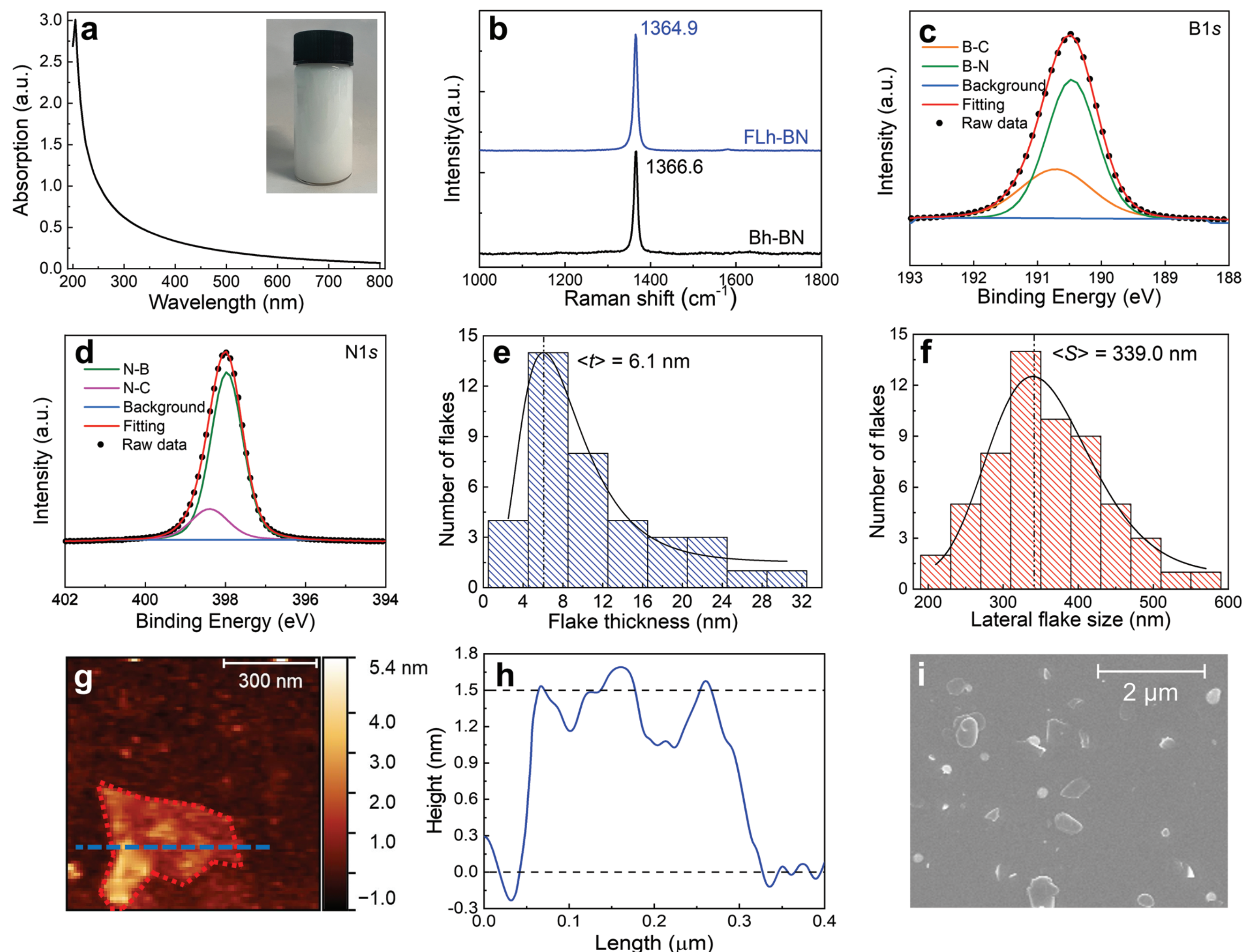

Figure 2. a) Optical absorption spectrum of the FLh-BN suspension, with an inset of the undiluted in the top right corner; b) Raman spectrum of the Bh-BN and the FLh-BN; High-resolution XPS spectrum of c) B1s and d) N1s of the FLh-BN; e) $<t>$ and f) $<S>$ distribution by AFM statistics of the FLh-BN flakes; g) A representative AFM image of a Mh-BN flake; h) The height profile of the Mh-BN flake in g); i) An SEM image of the FLh-BN flakes deposited on a Si/SiO_2 substrate.

substrate and a statistical analysis (shown Figure S1f, Supporting Information) over 34 flakes indicates an $<S> \approx 310$ nm, verifying the AFM statistics.

We performed thermogravimetric analysis (TGA)[72] to study the thermal stability properties of the Bh-BN/CMC composites at different compositions. **Figure 3a** shows the TGA curves plotting the sample weight loss as a function of temperature up to 500 °C. The weight of Bh-BN (black dotted curve) remained unchanged up to 500 °C, consistent with published results,[73] indicating that no decomposition of Bh-BN occurs for up to 500 °C. The weight of CMC (red dotted curve) started to decrease at ≈80 °C, reducing by ≈10% at ≈207 °C, which could be attributed to the presence of water moisture in the sample.[74] A more rapid decrease of the CMC weight down to ≈58% at 500 °C is attributed to the decarboxylation and pyrolysis of the cellulosic backbone.[74] Applying the first derivative of the TGA curve (Figure S1.2b, Supporting Information) we extracted the initial thermal decomposition temperature of the Bh-BN/CMC (Figure 3b) as a function of the Bh-BN loading. Introducing Bh-BN as a thermal filler into CMC increased the thermal decomposition temperature of the composite (Figure 3a,b) from 227 °C for pure CMC to 256 °C at 60 wt.%, indicating the improved thermal stability of the composite,[72] and allowed stabler heat dissipation at typical operating temperatures in power electronics.[75]

2.3. Thermal Performance of the Composites

The κ values of Bh-BN/CMC and FLh-BN/CMC were obtained using two different methods, steady-state method (SSM) and transient photothermal deflection technique (PDT). The SSM was performed with a physical properties measurement system (PPMS, Quantum Design) using a thermal transport option (TTO). In the SSM method, the sample was heated with a known steady-state heat flux (q), and the resulting temperature drops (ΔT) across a given length (Δx) of the sample were recorded after the system reached thermal equilibrium, from which we can obtain $\kappa_{SSM} = -q\Delta x/\Delta T$. This method is widely used for

© 2024 The Author(s). Advanced Functional Materials published by Wiley-VCH GmbH

16163028, 0, Downloaded from https://onlinelibrary.wiley.com/doi/10.1002/adfm.202405235 by CochraneItalia, Wiley Online Library on [14/07/2024]. See the Terms and Conditions (https://onlinelibrary.wiley.com/terms-and-conditions) on Wiley Online Library for rules of use; OA articles are governed by the applicable Creative Commons License

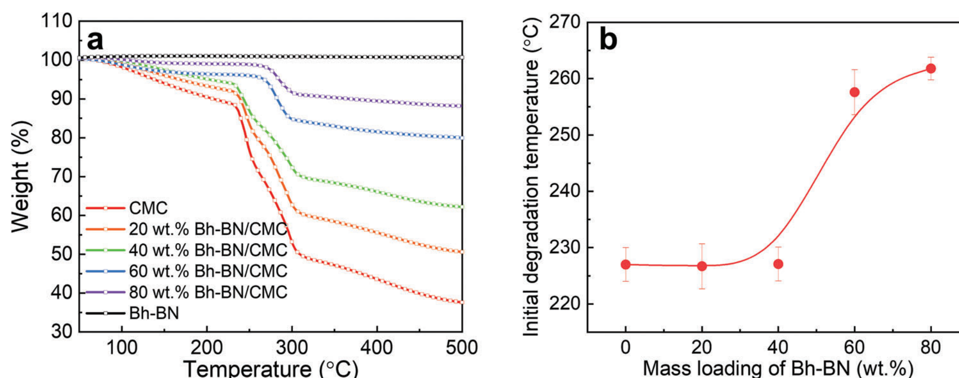

Figure 3. a) Thermogravimetric analysis profile, showing the decomposition of CMC (red dotted curve), Bh-BN (black dotted curve), and their composites at different compositions (20 wt.%: orange dotted curve; 40 wt.%: green dotted curve; 60 wt.%: blue dotted curve; and 80 wt.%: purple dotted curve) as a function of temperature; b) The initial decomposition temperature of Bh-BN/CMC as a function of the Bh-BN loading.

characterizing the κ of TIMs.[76] The PDT[77] applies a laser to the sample surface and records the thermal diffusion length (l_t) as a function of the laser frequency (F), obtaining the thermal diffusivity (D) of the sample. The κ value of the targeted sample can be determined by applying the equation $\kappa_{PDT} = \rho D C_p$, where ρ is the density and C_p is the specific heat capacity (determined via differential scanning calorimetry, DSC) of the measured sample (details in methods and Supporting Information).

Figure 4a shows the κ_{SSM} (black squares) and κ_{PDT} (red circles) values as a function of the mass loading of Bh-BN, from 0 wt.% to 90 wt.% for Bh-BN/CMC. Pure CMC (i.e., 0 wt.% Bh-BN mass loading) has a κ_{SSM} ≈1.4 W m^{-1} K^{-1} and κ_{PDT} ≈ 1.68 W m^{-1} K^{-1} respectively at room temperature. These are higher than the previously reported value of κ = 0.65 W m^{-1} K^{-1},[78] which we attribute to the water molecules trapped in the CMC reducing the air gap between the polymer chains and leading to a reduction of thermal contact resistance,[79] as evidenced by the 3% weight loss at ≈90 °C in Figure 3a. We note that a loading above 10 wt.% of Bh-BN into the CMC increases both κ_{SSM} and κ_{PDT}. A 20 wt.% loading of the Bh-BN into the CMC increases κ_{SSM} to ≈1.81 W m^{-1} K^{-1} and κ_{PDT} to ≈3.15 W m^{-1} K^{-1}, which corresponds to an enhancement of κ_{SSM} and κ_{PDT} by 29.3% and 87.5%,

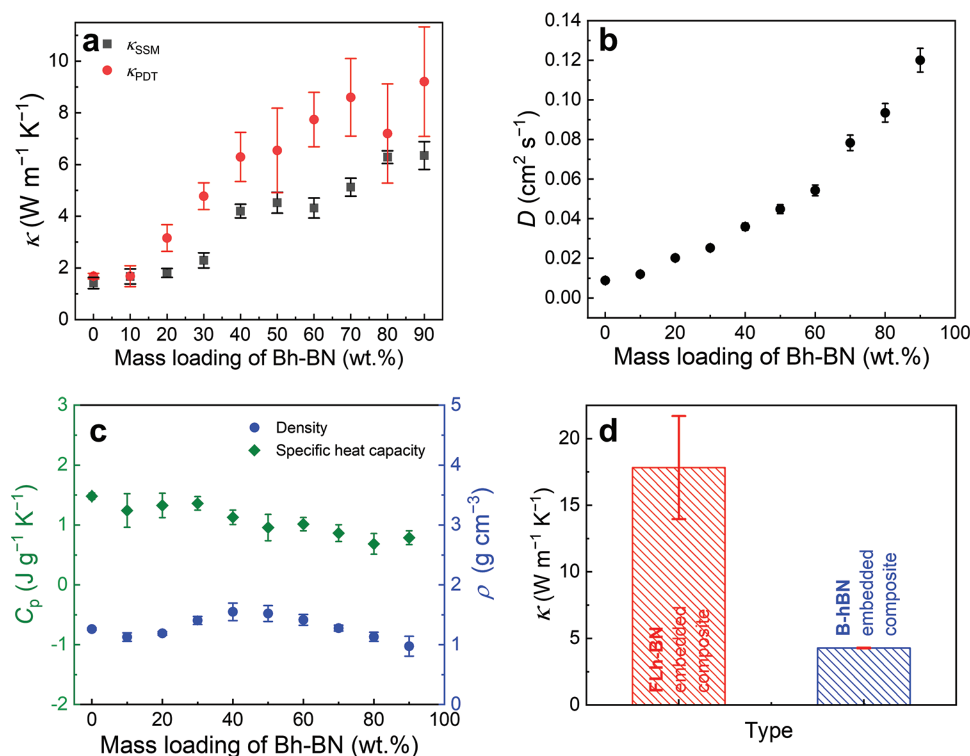

Figure 4. a) The κ values of Bh-BN/CMC using the SSM (black squares) and PDT (red circles) methods; b) the D of Bh-BN/CMC; c) the C_p (green diamonds) and the ρ (blue circles) of Bh-BN/CMC; d) the κ comparison of 60 wt.% Bh-BN/CMC and 60 wt.% FLh-BN/CMC.

© 2024 The Author(s). Advanced Functional Materials published by Wiley-VCH GmbH

16163028, 0, Downloaded from https://onlinelibrary.wiley.com/doi/10.1002/adfm.202405235 by Cochraneltalia, Wiley Online Library on [14/07/2024]. See the Terms and Conditions (https://onlinelibrary.wiley.com/terms-and-conditions) on Wiley Online Library for rules of use; OA articles are governed by the applicable Creative Commons License

respectively. A further increase of the Bh-BN mass loading in the composite to 50 and 90 wt.%, results in $\kappa_{SSM} \approx 4.4$ W m^{-1} K^{-1} and $\kappa_{SSM} \approx 6.4$ W m^{-1} K^{-1}, respectively, with the latter being almost an order of magnitude higher than that reported for CMC. In the same Bh-BN loading range, κ_{PDT} increased to ≈6.54 and ≈9.21 W m^{-1} K^{-1}, respectively. Both SSM and PDT data show a rapid increase in the 20–40 wt.% Bh-BN loading range pushing $\kappa_{SSM} \approx 4.2$ W m^{-1} K^{-1} and $\kappa_{PDT} \approx 6.3$ W m^{-1} K^{-1}, this corresponds to 132% and 100% increase respectively, before reaching a plateau after 60 wt.%. Such a rapid increase is the result of the Bh-BN loading reaching above the percolation threshold (i.e., 20 wt.%), meaning that a continuous thermal path across the Bh-BN flake network develops,[80] which forms effective phonon transmission channels while suppressing the phonon scattering caused by the Bh-BN/CMC interface.[81]

The difference between the SSM and the PDT data in the Bh-BN loading ranges 20 – 40 wt.%, and 60 – 70 wt.% is attributed to the inaccuracy of the emissivity estimation of the sample (resulting in an error of ≈±1 W m^{-1} K^{-1}) in the SSM system at room temperature,[55] at which the radiative heat losses are larger than those at low temperatures (<300 K). An additional thermal contact resistance per unit area of ≈40 K W^{-1} between the contact electrodes (silver epoxy on contact leads) and the sample causes an additional estimated $\kappa_{loss} \approx 2.0$ W m^{-1} K^{-1} at room temperature in the SSM system.[55]

Figure 4b shows the D values as a function of the mass loading of Bh-BN, from 0 to 90 wt.% for the Bh-BN/CMC (see Experimental Section). The value of D increases almost linearly up to 60 wt.% Bh-BN mass loading, with the increment becoming more rapid above 60 wt.% loading of Bh-BN. At 10 wt.% loading of Bh-BN, $D \approx 0.012$ cm^2 s^{-1}, while at 90 wt.% loading, it increases by 10 times to $D \approx 0.12$ cm^2 s^{-1}. Figure 4c shows the ρ and C_p values as a function of the mass loading of Bh-BN, from 0 to 90 wt.% for the Bh-BN/CMC. The C_p (green diamonds) values of the Bh-BN/CMC vary from $C_p \approx 1.5$ to ≈1 J g^{-1} K^{-1} as the Bh-BN loading increases, while ρ (blue circles) oscillates from $\rho \approx 1.27$ g cm^{-3} at 10 wt.% to $\rho \approx 1.55$ g cm^{-3} at 40 wt.%, and to $\rho \approx 0.98$ g cm^{-3} at 90 wt.% with a mean value of $\rho \approx 1.28$ g cm^{-3}. The slight decrease of the ρ above 40 wt.% loading of Bh-BN is attributed to the formation of larger gaps between flakes in the composites at higher Bh-BN loadings, which in turn increases their porosity, as observed in the SEM images (see Figure S5, Supporting Information). These values were used to estimate κ_{PDT} and their trend is in line with the trend seen for the κ_{SSM}.

From the comparison of κ_{SSM} and κ_{PDT} curves in Figure 4a we identify 60 wt.% as the minimum Bh-BN mass loading for the composite to reach maximum κ_{PDT}, representing an optimum loading value. We will then use this optimum mass loading value to compare Bh-BN and FLh-BN performance. Figure 4d compares the κ_{SSM} values of Bh-BN/CMC and FLh-BN/CMC (both at a mass loading at 60 wt.%). The 60 wt.% FLh-BN/CMC has as a mean $\kappa_{SSM} \approx 17.8$ W m^{-1} K^{-1}, with a maximum measure value of $\kappa_{SSM} \approx 21.7$ W m^{-1} K^{-1}. This is ≈5 times higher than the κ_{SSM} of the 60 wt.% Bh-BN/CMC ($\kappa_{SSM} \approx 4.5$ W m^{-1} K^{-1}), indicating the positive effect on κ of FLh-BN flakes. This is in line with the higher κ value reported for FLh-BN flakes compared to that of Bh-BN,[33] revealing that the FLh-BN flakes are promising thermally conducting fillers for TIMs.

2.4. Mechanical and Rheological Performance of the Composites

We performed tensile tests for the FLh-BN/CMC and Bh-BN/CMC dried pastes (**Figure 5**). Figure 5a plots the strain–stress curves of the composites at different Bh-BN loadings and 60% FLh-BN loading for comparison. Figure 5b summarizes the tensile strengths (P) and Young's modulus (ε) values of the same composites. We measure $P \approx 18.30$ MPa (black dotted curve) for pure CMC, which increases by 119% to $P \approx 40.01$ MPa (orange dotted curve) with a 40 wt.% loading of Bh-BN, due to the improved interfacial adhesion between the filler (h-BN) and the matrix (CMC). The strength of the composite at 60 wt.% Bh-BN loading decreases to $P \approx 19.44$ MPa (red dotted curve) but it is still 6.3% higher than that of CMC. This can be attributed to the interruption of the polymer crosslinking in the presence of excess filler.[82] Similarly, the 60 wt.% FLh-BN/CMC composite achieves $P \approx 20.77$ MPa (blue dotted curve) which is 13.6% higher than that of CMC. Inclusion of 60 wt.% Bh-BN or FLh-BN increases ε of the composite from ≈1.0 to ≈1.8 GPa and ≈1.5 GPa, respectively. We then characterized the rheological properties of 60 wt.% FLh-BN/CMC (blue dots) and 60 wt.% Bh-BN/CMC (red dots) composites in the form of thermal pastes. Figure 5c shows η values as a function of shear rate γ (s^{-1}) for both samples. The pastes have a η of 273 584 and 674 806 mPa s, respectively, at 0.017 s^{-1} (1 rpm), which both fall within the η range (10^4–10^6 mPa s) of commercial thermal pastes.[83–85]

2.5. Heat Dissipation Results of the Composites as Thermal Pastes

We built a temperature-monitoring setup (**Figure 6a**) to demonstrate the practical feasibility of the Bh-BN/CMC and FLh-BN/CMC pastes as TIMs on a hot surface and the enhanced heat dissipation of the FLh-BN/CMC paste over the Bh-BN/CMC one.

The setup is composed of a heat generation component (a resistance heater powered by a power supply), a heat conduction component (the Bh-BN/CMC and FLh-BN/CMC pastes), a heat dissipation component (a heat sink coupled with a fan), and a temperature monitoring system (K-type thermocouples with a temperature data logger). For each paste, we uniformly coated via a blade the as-prepared paste to one side of the resistance heater, ensuring a thickness of the paste layer of 1 mm. The thermocouples were inserted at the surface of the heater to monitor the temperature change and temperature distribution, and the fan was applied to ensure constant and sufficient heat dissipation. The heat was generated by forcing a current through the heater, and when the system reached thermal equilibrium. The T_{max} and the minimum temperature (T_{min}) measured on the surface of the resistance heater, and the temperature uniformity across the area of the whole resistance heater ($\Delta T = T_{max} - T_{min}$, Figure 6e) were recorded and compared.

Figure 6b shows the T_{max} as a function of the increasing mass loading of Bh-BN in the pastes, at a heat power density (h) of 1.24 W cm^{-2}. When no paste is applied, the initial $T_{max,i} \approx 123.4$ °C. When applying the pure CMC paste as a TIM, we measure a stable $T_{max} \approx 55.4$ °C. By increasing the Bh-BN mass loading to 60 wt.%, we notice a drop to $T_{max} \approx 39.9$ °C, with a maximum drop to $T_{max} \approx 33.4$ °C at 80 wt.% mass loading. Increasing

© 2024 The Author(s). Advanced Functional Materials published by Wiley-VCH GmbH

16163028, 0, Downloaded from https://onlinelibrary.wiley.com/doi/10.1002/adfm.202405235 by Cochraneltalia, Wiley Online Library on [14/07/2024]. See the Terms and Conditions (https://onlinelibrary.wiley.com/terms-and-conditions) on Wiley Online Library for rules of use; OA articles are governed by the applicable Creative Commons License

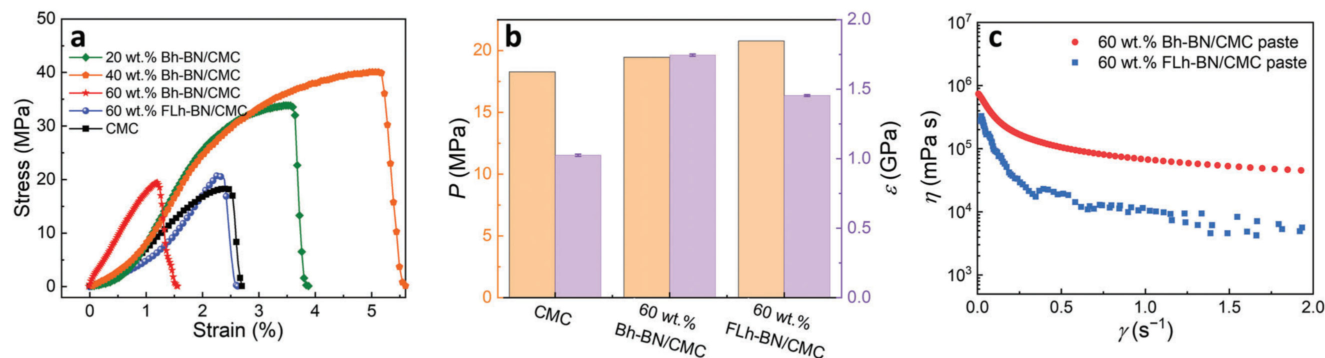

Figure 5. Mechanical properties of FLh-BN/CMC and Bh-BN/CMC composites, including a) strain–stress curves of FLh-BN/CMC and Bh-BN/CMC composites; b) a column chart summarizing their P and ε values; c) η of 60 wt.% FLh-BN/CMC and 60 wt.% Bh-BN/CMC pastes.

Figure 6. a) Configuration and assembly of the custom-built temperature monitoring setup, b) the T_{max} performance of the Bh-BN/CMC at different mass loadings, c) real-time temperature evolution of the heater using different thermal pastes at 1.24 W cm^{-2}, d) T_{max}, and e) ΔT of the 60 wt.% FLh-BN/CMC compared with that of the 60 wt.% Bh-BN/CMC, at different heat generation densities; (f) real-time temperature evolution of the heater using the FLh-BN/CMC paste at different air convection rates, at 1.24 W cm^{-2} and g) the radar plot comparing key parameters of the FLh-BN/CMC paste compared to commercial thermal pastes.[86,87]

© 2024 The Author(s). Advanced Functional Materials published by Wiley-VCH GmbH

16163028, 0, Downloaded from https://onlinelibrary.wiley.com/doi/10.1002/adfm.202405235 by CochraneItalia, Wiley Online Library on [14/07/2024]. See the Terms and Conditions (https://onlinelibrary.wiley.com/terms-and-conditions) on Wiley Online Library for rules of use; OA articles are governed by the applicable Creative Commons License

16163028, 0, Downloaded from https://onlinelibrary.wiley.com/doi/10.1002/adfm.202405235 by CochraneItalia, Wiley Online Library on [14/07/2024]. See the Terms and Conditions (https://onlinelibrary.wiley.com/terms-and-conditions) on Wiley Online Library for rules of use; OA articles are governed by the applicable Creative Commons License

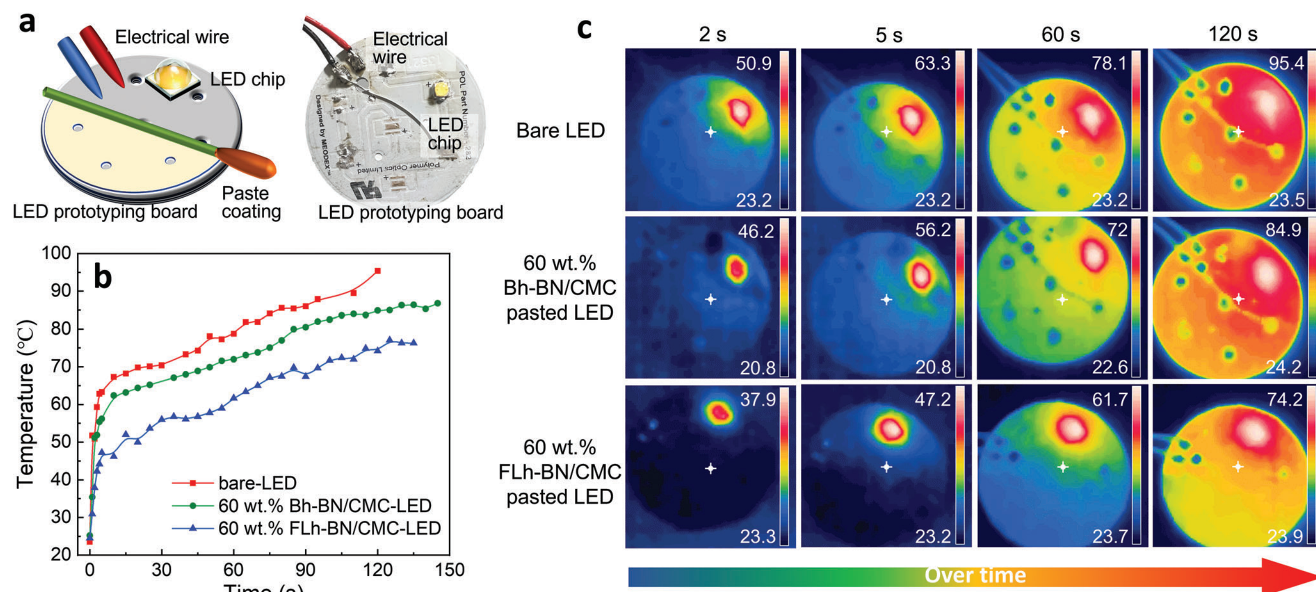

Figure 7. Use of the as-prepared pastes for heat dissipation enhancement of a high-power LED chip: a) schematic illustration of a soldered LED chip with attached pastes and a real test image; b) the recorded LED core temperature evolution over time without (red squares) and with (green circles: Bh-BN/CMC; blue triangles: FLh-BN/CMC) the pastes, g) infrared thermal images of temperature evolution of the soldered LED chip over time.

the mass loading of Bh-BN in the paste results in a decrease in the T_{max} of the heater, due to the improved κ value at a higher Bh-BN loading as shown in Figure 4a.

Figure 6c shows a real-time temperature evolution of the heater using the FLh-BN/CMC in comparison to a Bh-BN/CMC paste at 1.24 W cm^{-2}. showing the benefit of the T_{max} drop brought by the FLh-BN/CMC paste. Figure 6d,e summarizes a comparison of the T_{max} and ΔT of the heater coated with the Bh-BN/CMC paste (red squares) and FLh-BN/CMC (blue circles) paste at 60 wt.% mass loading, as a function of h. At $h = 1.24$ W cm^{-2}, applying the Bh-BN/CMC, we obtain $T_{max} \approx 39.9$ °C with a corresponding $\Delta T \approx 8.3$ °C, while applying the FLh-BN/CMC $T_{max} \approx 27.8$ °C and $\Delta T \approx 3.1$ °C, respectively. This corresponds to a T_{max} reduction of >30%. The reduction in both the T_{max} and ΔT values brought by the 60 wt.% FLh-BN/CMC paste is more significant at higher h, as shown in Figure 6d,e. At $h = 2.48$ W cm^{-2}, applying the FLh-BN/CMC, T_{max} was reduced by 40% from ≈57.7 to ≈33.2 °C (equivalent to a temperature drop of ≈24.5 °C) and ΔT from 15.1 to 5.9 °C (≈9.2 °C), compared to the Bh-BN/CMC paste. This result corresponds to ≈40% reduction in T_{max} and it is a direct effect of the fivefold higher κ of the FLh-BN/CMC than that of Bh-BN/CMC and shows a clear advantage in a typical application of TIMs. With the aim to simulate real heat management in electronic components, we use a fan to vary the airflow of a 60 wt.% FLh-BN coated heat resistor. Figure 6f shows the temperature evolution as a function of time for two different air velocities (namely 1.8 and 3.6 m s^{-1}) demonstrating that the T_{max} of the heater still remains below 30 °C with a lower air velocity (resulting in a lower energy consumption) at 1.8 m s^{-2} and with a minimum contribution of the cooling fan.

Figure 6g shows a radar plot comparing the key parameters of the FLh-BN/CMC paste compared to two commercial thermal pastes (Electrolube TCOR and DeltaBond).[86,87] Our FLh-BN/CMC paste shows a higher κ (21.7 W m^{-1} K^{-1}), higher η (273584 mPa s), stronger tensile strength, P (20.77 MPa), larger specific volume (lower density, $1/\rho \approx 0.64$ cm^3 g^{-1}), and stronger breakdown strength (14.6 kV mm^{-1}) than the two commercial pastes, indicating its high commercial viability.

Figure 7a demonstrates the benefit of using the FLh-BN/CMC and Bh-BN/CMC pastes to reduce the T_{max} of an operating high-power LED chip. The LED was mounted on an LED prototyping board (Part No.—282, Polymer Optics) and biased with a voltage of 3.2 V and a current of 1.4 A. Figure 7b shows that during the normal LED operation, the T_{max} around the LED area reached 95.4 °C after an operation time of 120 s, as demonstrated in Figure 7c. When the 60 wt.% Bh-BN/CMC paste or the 60 wt.% FLh-BN/CMC paste was coated on the LED prototyping board, the maximum temperature of the LED chip decreased to 84.9 and 74.2 °C at 120 s, respectively. The resulting ≈21 °C decrease in the LED temperature when the circuit board is coated with the FLh-BN coating is a clear evidence of the heat dissipation ability of our h-BN pastes.

3. Conclusion

In this work, we demonstrate few layer h-BN/cellulose composites as promising thermally interface materials, such as commercial thermal pastes in electronics. Comparing bulk h-BN/cellulose composites to few-layer h-BN ones, obtained by liquid phase exfoliation of bulk h-BN, we show that the thermal conductivity, κ of bulk h-BN composites can reach $\kappa \approx 6.35$ W m^{-1} K^{-1} as a function of h-BN mass loading, while an extraordinary $\kappa \approx 21.7$ W m^{-1} K^{-1} is achieved with few-layer h-BN flakes embedded into cellulose at a mass loading of 60 wt.%. This is more than a fivefold improvement over the κ value of bulk h-BN embedded cellulose composites. We finally demonstrate a clear advantage in two typical applications in the form of thermal pastes as thermal interface materials, by showing that the

© 2024 The Author(s). Advanced Functional Materials published by Wiley-VCH GmbH

few-layerh-BN embedded composite can reduce the maximum temperature of a heating pad at $h = 2.48$ W cm^{-2} by ≈24.5 °C, and reduce the maximum temperature by 9 °C of an operating high power LED chip, than what bulk h-BN composites can do at the same h-BN loading. Our results provide an effective approach to improving κ value of cellulose-based composite materials for heat dissipation in integrated circuits and high-power electronic devices.

4. Experimental Section

Formulation of LPE FLh-BN Suspension: A 50 mg mL^{-1} Bh-BN powder (Goodfellows B516011, <10 µm size) was added to 3 mg mL^{-1} CMC (average $M_W = 700\,000$) in a co-solvent system which was mixed with 45 vol.% deionized water and 55 vol.% ethanol (Sigma Aldrich, ACS reagent ≥ 99.8% purity). The mixture was then processed by a probe sonicator (Branson SFX550, 101-148-062) at 120 W for 3 h. The resulting dispersion was subsequently centrifuged (Beckman Allegra 64R, F06050, Fixed-Angle Rotor)) at 3000 rpm for 30 min to remove any unexfoliated h-BN flakes. After the centrifugation, the supernatant (i.e., top 70%) was retained as the FLh-BN suspension.

Bh-BN/CMC Paste Preparation: The Bh-BN/CMC composites were prepared via simple vortex mixing. First, the amount of Bh-BN and CMC powders was weighed using a microbalance (KERN ABT IOO-5NM) to determine different loading amounts of Bh-BN in the composite. Then, the two powders were placed in a vial and mixed via vortex (F20210176FI, Fisherbrand) for 5 min to produce a homogenous mixture. The powder mixture was compressed at 15 tons for 30 min using a hydraulic press (Specac Atlas 15T) and was subsequently dissolved in water, to form a viscous paste. The paste was shaped into a rod (13 mm in diameter) to create a symmetrical structure for κ measurements.

FLh-BN/CMC Paste Preparation: The FLh-BN/CMC composite was prepared by mixing a 3 mg mL^{-1} CMC aqueous solution with the FLh-BN suspension via stirring. The FLh-BN suspension was produced via ultrasonication-assisted LPE, which is described in the *Formulation of LPE FLh-BN suspension*. The two suspensions were mixed and stirred on a hot plate (MS-H280-Pro) for 1 h. The mixture was formed into a flexible thin film via evaporation-induced self-assembly and rolled into a rod suitable for κ measurements.

Optical Absorption Spectroscopy: The concentration of the FLh-BN suspension was obtained via the Beer-Lambert Law, which correlates the absorbance $A = \alpha cl$, with the beam path length l (m), the concentration c (g L^{-1}), and the absorption coefficient α (L g^{-1} m^{-1}). The FLh-BN suspension was diluted at 1:100 with the co-solvent (water/ethanol) and optically characterized using a UV-Vis-NIR spectrophotometer (Agilent Cary 60). The absorption coefficient of $\alpha = 2350$ L g^{-1} m^{-1} at 300 nm[62] was utilized.

Raman Spectroscopy: Thin films of Bh-BN and FLh-BN were deposited on the Si/SiO_2 substrate, and the Raman spectrum was acquired by a Renishaw in Via micro-Raman spectrometer (WiRe 4.1) using a green 532 nm laser and a ×50 objective, with an incident power of below 1 mW to avoid possible thermal damage.

Atomic Force Microscopy (AFM): The FLh-BN suspension was diluted to 0.01 mg mL^{-1} and drop-casted onto a pre-cleaned (cleaned with acetone and isopropanol and treated with Ozone) Si/SiO_2 substrate. Measurements were scanned on a 10 µm × 10 µm area of the prepared sample, using an Asylum MFP-3D AFM (Oxford Instruments) with a silicon tip (NuNano Scout 70) in a tapping mode, with a 70 kHz resonance frequency and tip radius curvature of <10 nm. AFM statistical analysis collected on 38 flakes was carried out to reveal the $<t>$ distribution and $<S>$ distribution of the FLh-BN flakes. The $<S>$ was obtained via $<S> = xy^{0.5}$, where x and y refer to the length and width of a particular FLh-BN flake. The aspect ratio of a FLh-BN flake was defined as $<S>/<t>$.

Scanning Electron Microscopy (SEM): The SEM images were acquired using a Zeiss LEO Gemini 1525 FEG-SEM and collected in a secondary electron detection mode using the In Lens and SE2 detectors.

X-ray Photoelectron Spectroscopy (XPS): XPS spectrum were acquired using the Thermo Scientific K-Alpha system incorporating a micro-focused Al Kα X-ray source. The etching (profiling) was performed using the built-in argon ion sputtering gun, at 500 eV cluster energy and "medium" current setting, with an ≈0.08 nm s^{-1} etch rate.

Thermogravimetric Analysis (TGA) and Differential Scanning Calorimetry (DSC): TGA and DSC were performed using a Netzsch 449 F5 under an Ar/H_2 atmosphere with a flow rate of 50 mL min^{-1}, starting from room temperature up to 500 °C at a heating rate of 5 K min^{-1}. Samples were placed in a 70 µL Platinum (PtRh 80:20%) crucible (Mettler Toledo, ME-51119654) and another empty platinum crucible was used as the reference. Baseline correction was applied to remove any impact from the ambient environment (vibration, humidity, etc.). The C_p was obtained using the standard Sapphire method applying the equation $C_{ps} = C_{pr} \times \Delta H \times m_r / (\Delta h \times m_s)$, where C_{ps} and C_{pr} (J g^{-1} K^{-1}) refer to the C_p of the sample and the reference material (Sapphire), m_r and m_s (kg) refer the mass of the sample and the Sapphire, ΔH, and Δh (W) refer to the corrected heat flow characteristics of the sample and the Sapphire, respectively. The Sapphire has a geometry of 5.2 mm in diameter and 0.25 mm in thickness, which has a similar heat mass compared with the samples to the best accuracy of C_p determination.

Steady-State Thermal Conductivity Measurement (SSM): The SSM was performed at a PPMS (DynaCool System, Quantum Design) with a TTO (DynaCool CAN-based D670, Quantum Design). Samples were mounted on a TTO puck, using a four-probe lead configuration. The leads connected the sample to a heater, a hot temperature sensor, a cold temperature sensor, and a coldfoot, respectively. A conductive adhesive (silver conductive paint SCP03B, Electrolube) was applied to reduce the thermal contact resistance between the leads and the sample. The puck was covered by an isothermal radiation shield to reduce the radiation loss. The measurements were operated under a high vacuum from 275 to 325 K. The κ values were obtained by applying the equation $\kappa = -q\Delta x/\Delta T$, where the steady-state heat flux input (q) and the resulting temperature drop (ΔT) across a given length (Δx) of the sample were recorded after the thermal equilibrium was established.

Density: The densities of the composites were obtained applying the equation $\rho = m/V$, where the mass (m) was weighed using a micro-balance (KERN ABT IOO-5NM) and the volume (V) was obtained via multiplying the cross-sectional area of the sample to its height.

Photothermal Deflection Technique (PDT): The PDT[77] used a 488 nm Ar laser with a power of 50 mW as a pump beam and a He-Ne laser focused close to the surface of the sample at a 0.04 mm spot-size as a probe beam. The measurements were performed at 6 pump F values as a function of the pump-probe distance (Y). The l_t was obtained from the linear part of the phase toward Y. With plotting l_t as a function of $F^{-0.5}$ and obtaining the slope values, the D value of the sample was obtained applying the equation $D = \pi F (l_t)^2$. The PDT setup was corrected and validated by measuring the D of GaAs at 0.22 cm^2 s^{-1} at the frequency of 81 Hz. Details can be found in the Supporting Information.

Heat Dissipation Effects Measurement: A custom-built temperature monitoring setup was used to record the real-time temperature change of the resistance heater (Vishay Resistor, LTO150F4R700JTE3, thermal resistance of 1.5 K W^{-1}) applying a TIM. The setup consists of a heat generation component (a resistance heater powered by a DC power supply(RS PRO RS3005D)), a heat conduction component (TIMs to be tested in this work), a heat dissipation component (a heat sink and couple with a fan (Thermoelectric devices, TDEX3132/100/FMF12G)), and a temperature monitoring system (K-type thermocouples with a temperature data logger (TASI, TA612C) as cooling components. For each paste, it was attached the as-prepared paste to one side of the resistance heater, using the heat sink to press manually from the upper side and ensuring a thickness of the paste layer at 1 mm (the 1 mm gap was controlled in the control test without attaching the TIM). The fan was placed at the side of the heat sink to ensure constant and sufficient heat dissipation. Thermocouples were inserted at the surface of the heater to monitor the temperature change and temperature distribution when the system reached thermal equilibrium. The temperature evolution of an operating high power LED chip (ams OSRAM, GW CSSRM3) with and without paste

© 2024 The Author(s). Advanced Functional Materials published by Wiley-VCH GmbH

16163028, 0, Downloaded from https://onlinelibrary.wiley.com/doi/10.1002/adfm.202405235 by Cochraneltalia, Wiley Online Library on [14/07/2024]. See the Terms and Conditions (https://onlinelibrary.wiley.com/terms-and-conditions) on Wiley Online Library for rules of use; OA articles are governed by the applicable Creative Commons License

attached was recorded using an infrared thermal imaging camera (UNI-T UTi120S).

Rheology Tests: The η measurement was performed using HAAKE MARS 60 with a P35-geometry parallel plate. A 1 mL paste was attached to the lower plate and covered with the upper plate. A range of shear rates from 0.01 to 2.0 s^{-1} was applied to the paste. The choice of the range of the shear rate is based on literature values (0–10 rpm, or 0–2 s^{-1}).

Tensile Tests: The tensile tests were performed using a custom-built apparatus with an enclosed container (Waysafe GP540), a Retro-Fit variable speed controller (2100-REE10, Solotec), and a modular force tensile stage (Linkam MFS system). The composite was fixed using an epoxy (Araldite Rapid) at two ends to a paper strip and cured at room temperature for a week, resulting in a test length of 15 mm. A single pull-out test was carried out using a force beam of 20 N with a force resolution of 0.1 mN operated at 16.67 µm s^{-1}, and the force (N) as a function of extension (mm) of the composites was recorded. The P (MPa) was calculated from the force per cross-sectional area and the strain (%) was equal to the extension in sample length divided by its original length.

Supporting Information

Supporting Information is available from the Wiley Online Library or from the author.

Acknowledgements

The authors acknowledge funding from the European Union (NextGeneration EU), through the MUR-PNRR project SAMOTHRACE (ECS00000022). F.T., C.Y., M.H., S.L., and B.F.S, acknowledge funding from EPSRC via grants EP/P02534X/2, EP/T005106/1, EP/R511547/1, EP/X026876/1. C.Y. acknowledges the funding support from the Department of Chemistry, Imperial College London, and the China Scholarship Council. F.T. and Maria Cristina L. also acknowledge the support from the University La Sapienza for the Visiting Professor Program 2021 (Bando Professori Visitatori 2021). The authors would like to acknowledge the support from the Henry Royce Institute for advanced materials through the Equipment Access Scheme enabling access to Royce facilities at Cambridge (Cambridge Royce Facilities Grant EP/P024947/1 and Sir Henry Royce Institute – Recurrent Grant EP/R00661X/1). C.Y. is grateful for the support of Dr. Hyunho Kim and Dr. Cheng Liu in running the PPMS measurements and of Shawn Jinhau Lew in performing rheology tests.

Conflict of Interest

The authors declare no conflict of interest.

Author Contributions

C.Y. conceived and conducted the experiments, analyzed the results, and contributed to result interpretation and procedural validation; C.Y. also conducted the literature search and the characterization of materials; F.T. directed the project and contributed to result interpretation and procedural validation; G.L. performed the thermal diffusivity tests under the supervision of Maria Cristina L., R.L.V., and C.S.; M.H. performed the XPS tests; S.L. performed the Raman spectroscopy and B.F.S. performed the SEM of FLh-BN; May Ching L. performed the SEM of the composites; C.D. and G.D. contributed to the SEM experiment design and advised on the SEM data analysis; C.Y. and F.T. wrote the manuscript with input from all the authors.

Data Availability Statement

The data that support the findings of this study are available from the corresponding author upon reasonable request.

Keywords

heat dissipation, hexagonal boron nitride, packaging, thermal conductivity, thermal interface materials, thermal management

Received: March 26, 2024
Revised: May 31, 2024
Published online:

[1] Z. Zhang, X. Wang, Y. Yan, *e-Prime-Adv. Electr. Eng., Electron. Energy.* **2021**, *1*, 100009.
[2] D. Dan, C. Yao, Y. Zhang, Y. Qian, W. Zhuge, *Chin. Sci. Bull.* **2019**, *64*, 682.
[3] C. Yao, D. Dan, Y. Zhang, Y. Wang, Y. Qian, Y. Yan, W. Zhuge, *Automot. Innovation* **2020**, *3*, 317.
[4] M. Hamidnia, Y. Luo, X. D. Wang, *Appl. Therm. Eng.* **2018**, *145*, 637.
[5] A. L. Moore, L. Shi, *Mater. Today* **2014**, *17*, 163.
[6] I. Afaynou, H. Faraji, K. Choukairy, A. Arshad, M. Arıcı, *Int. Commun. Heat Mass Transfer* **2023**, *143*, 106690.
[7] K. M. Razeeb, E. Dalton, G. L. W. Cross, A. J. Robinson, *Int. Mater. Rev.* **2018**, *63*, 1.
[8] C. J. Lasance, R. E. Simons, *Electron. Cool.* **2005**, *11*, 22.
[9] M. Grujicic, C. L. Zhao, E. C. Dusel, *Appl. Surf. Sci.* **2005**, *246*, 290.
[10] J. Zhang, H. Zhai, Z. Wu, Y. Wang, H. Xie, M. Zhang, *Energy Rep.* **2020**, *6*, 116.
[11] C. Guo, Y. Li, J. Xu, Q. Zhang, K. Wu, Q. Fu, *Mater. Horiz.* **2022**, *9*, 1690.
[12] C. P. Feng, L. Y. Yang, J. Yang, L. Bai, R. Y. Bao, Z. Y. Liu, M. B. Yang, H. B. Lan, W. Yang, *Compos. Commun.* **2020**, *22*, 100528.
[13] Q. He, M. Qin, H. Zhang, J. Yue, L. Peng, G. Liu, Y. Feng, W. Feng, *Mater. Horiz.* **2024**, *11*, 531.
[14] H. Ma, B. Gao, M. Wang, Z. Yuan, J. Shen, J. Zhao, Y. Feng, *J. Mater. Sci.* **2021**, *56*, 1064.
[15] T. Zhou, X. Wang, X. Liu, D. Xiong, *Carbon* **2010**, *48*, 1171.
[16] Z. Yuan, H. Ma, M. A. Hussien, Y. Feng, *Macromol. Mater. Eng.* **2021**, *306*, 2100428.
[17] Y. Zhou, S. Wu, Y. Long, P. Zhu, F. Wu, F. Liu, V. Murugadoss, W. Winchester, A. Nautiyal, Z. Wang, Z. Guo, *ES Mater. Manuf.* **2020**, *7*, 4.
[18] Y. Zhang, J. Ma, N. Wei, J. Yang, Q. X. Pei, *Phys. Chem. Chem. Phys.* **2021**, *23*, 753.
[19] S. Choi, J. Kim, *Composites, Part B* **2013**, *51*, 140.
[20] T. Yamane, N. Nagai, S. I. Katayama, M. Todoki, *J. Appl. Phys.* **2002**, *91*, 9772.
[21] H. Li, L. Wang, Y. He, Y. Hu, J. Zhu, B. Jiang, *Appl. Therm. Eng.* **2015**, *88*, 363.
[22] Y. Yao, X. Zeng, G. Pan, J. Sun, J. Hu, Y. Huang, R. Sun, J. B. Xu, C. P. Wong, *ACS Appl. Mater. Interfaces* **2016**, *8*, 31248.
[23] H. Q. Xie, J. C. Wang, T. G. Xi, Y. Liu, *Int. J. Thermophys.* **2002**, *23*, 571.
[24] Z. Shi, M. Radwan, S. Kirihara, Y. Miyamoto, Z. Jin, *Appl. Phys. Lett.* **2009**, *95*, 224104.
[25] Y. Ji, S. D. Han, H. Wu, S. Y. Guo, F. S. Zhang, J. H. Qiu, *Chin. J. Polym. Sci.* **2024**, *42*, 352.
[26] J. M. Hutchinson, S. Moradi, *Materials* **2020**, *13*, 3634.
[27] Y. Cui, Z. Qin, H. Wu, M. Li, Y. Hu, *Nat. Commun.* **2021**, *12*, 1284.
[28] W. Xing, Y. Xu, C. Song, T. Deng, *Nanomaterials* **2022**, *12*, 3365.
[29] X. C. Tong, *Advanced Materials For Thermal Management Of Electronic Packaging*, Springer Science & Business Media, IL, USA **2011**.
[30] E. K. Sichel, R. E. Miller, M. S. Abrahams, C. J. Buiocchi, *Phys. Rev. B* **1976**, *13*, 4607.
[31] T. Ouyang, Y. Chen, Y. Xie, K. Yang, Z. Bao, J. Zhong, *Nanotechnology* **2010**, *21*, 245701.

© 2024 The Author(s). Advanced Functional Materials published by Wiley-VCH GmbH

16163028, 0, Downloaded from https://onlinelibrary.wiley.com/doi/10.1002/adfm.202405235 by CochraneItalia, Wiley Online Library on [14/07/2024]. See the Terms and Conditions (https://onlinelibrary.wiley.com/terms-and-conditions) on Wiley Online Library for rules of use; OA articles are governed by the applicable Creative Commons License

[32] C. Yuan, J. Li, L. Lindsay, D. Cherns, J. W. Pomeroy, S. Liu, J. H. Edgar, M. Kuball, *Commun. Phys.* **2019**, *2*, 43.
[33] C. Wang, J. Guo, L. Dong, A. Aiyiti, X. Xu, B. Li, *Sci. Rep.* **2016**, *6*, 25334.
[34] Q. Cai, D. Scullion, W. Gan, A. Falin, S. Zhang, K. Watanabe, T. Taniguchi, Y. Chen, E. J. Santos, L. H. Li, *Sci. Adv.* **2019**, *5*, eaav0129.
[35] P. Jiang, X. Qian, R. Yang, *Rev. Sci. Instrum.* **2017**, *88*, 074901.
[36] *Chemtronics, CircuitWorks Boron Nitride Heat Sink Grease*, https://docs.rs-online.com/a6fa/0900766b8172a9cb.pdf, (accessed: March 2024).
[37] L. Technologies, *T-flex™ 600 Series Thermal Gap Filler*, https://docs.rs-online.com/d9b4/0900766b80b192eb.pdf. (accessed: March 2024).
[38] 3M Advanced Materials Division, 3MTM Bornitrid Cooling Fillers, for thermally conductive and electrically insulating plastics and adhesives, (accessed: March 2024).
[39] Z. B. Zhao, C. Hu, Y. Wang, H. M. Cong, Y. Ma, D. D. Lin, W. L. Li, C. Yan, *Ceram. Int.* **2022**, *48*, 28030.
[40] X. Xu, R. Hu, M. Chen, J. Dong, B. Xiao, Q. Wang, H. Wang, *Chem. Eng. J.* **2020**, *397*, 125447.
[41] K. Kim, J. Kim, *Int. J. Therm. Sci.* **2016**, *100*, 29.
[42] J. Han, G. Du, W. Gao, H. Bai, *Adv. Funct. Mater.* **2019**, *29*, 1900412.
[43] Z. G. Wang, M. Z. Chen, Y. H. Liu, H. J. Duan, L. Xu, L. Zhou, J. Z. Xu, J. Lei, Z. M. Li, *J. Mater. Chem. C* **2019**, *7*, 9018.
[44] R. C. Zhang, Z. Huang, Z. Huang, M. Zhong, D. Zang, A. Lu, Y. Lin, B. Millar, G. Garet, J. Turner, G. Menary, *Compos. Sci. Technol.* **2020**, *196*, 108154.
[45] T. Carey, S. Cacovich, G. Divitini, J. Ren, A. Mansouri, J. M. Kim, C. Wang, C. Ducati, R. Sordan, F. Torrisi, *Nat. Commun.* **2017**, *8*, 1.
[46] Y. H. Jung, T. H. Chang, H. Zhang, C. Yao, Q. Zheng, V. W. Yang, H. Mi, M. Kim, S. J. Cho, D. W. Park, H. Jiang, *Nat. Commun.* **2015**, *6*, 7170.
[47] H. Zhu, Z. Fang, C. Preston, Y. Li, L. Hu, *Energy Environ. Sci.* **2014**, *7*, 269.
[48] G. Angeles, M. Lascurain, R. Davalos-Sotelo, R. P. Zarate-Morales, F. Ortega-Escalona, *Am. J. Bot.* **2013**, *100*, 1509.
[49] J. Cha, J. Kim, S. Ryu, S. H. Hong, *Composites, Part B* **2019**, *162*, 283.
[50] Q. F. Guan, H. B. Yang, Z. M. Han, L. C. Zhou, Y. B. Zhu, Z. C. Ling, H. B. Jiang, P. F. Wang, T. Ma, H. A. Wu, S. H. Yu, *Sci. Adv.* **2020**, *6*, eaaz1114.
[51] E. Foo, M. Jaafar, A. Aziz, L. C. Sim, *Composites, Part A* **2011**, *42*, 1432.
[52] A. Lund, Y. Wu, B. Fenech-Salerno, F. Torrisi, T. B. Carmichael, C. Müller, *MRS Bull.* **2021**, *46*, 491.
[53] X. Zeng, J. Sun, Y. Yao, R. Sun, J. B. Xu, C. P. Wong, *ACS Nano* **2017**, *11*, 12.
[54] X. Tian, N. Wu, B. Zhang, Y. Wang, Z. Geng, Y. Li, *Chem. Eng. J.* **2021**, *408*, 127360.
[55] Q. Design, *Thermal Transport Option User's Manual*, Quantum Design Inc., San Diego, CA **2002**.
[56] Z. Rafiei-Sarmazdeh, S. H. Jafari, S. J. Ahmadi, S. M. Zahedi-Dizaji, *J. Mater. Sci.* **2016**, *51*, 3162.
[57] T. Sato, R. Ruch, Stabilization of Colloidal Dispersions By Polymer Adsorption **1980**.
[58] J. Kang, J. W. T. Seo, D. Alducin, A. Ponce, M. J. Yacaman, M. C. Hersam, *Nat. Commun.* **2014**, *5*, 5478.
[59] S. Qiang, T. Carey, A. Arbab, W. Song, C. Wang, F. Torrisi, *Nanoscale* **2019**, *11*, 9912.
[60] H. Kim, A. Arbab, B. Fenech-Salerno, C. Yao, R. Macpherson, J. M. Kim, F. Torrisi, *Nanotechnology* **2022**, *33*, 215704.
[61] Y. Hernandez, V. Nicolosi, M. Lotya, F. M. Blighe, Z. Sun, S. De, I. T. McGovern, B. Holland, M. Byrne, Y. K. Gun'Ko, J. J. Boland, *Nat. Nanotechnol.* **2008**, *3*, 563.
[62] J. Shen, Y. He, J. Wu, C. Gao, K. Keyshar, X. Zhang, Y. Yang, M. Ye, R. Vajtai, J. Lou, P. M. Ajayan, *Nano Lett.* **2015**, *15*, 5449.
[63] R. V. Gorbachev, I. Riaz, R. R. Nair, R. Jalil, L. Britnell, B. D. Belle, E. W. Hill, K. S. Novoselov, K. Watanabe, T. Taniguchi, A. K. Geim, *Small* **2011**, *7*, 465.
[64] P. K. Rastogi, K. R. Sahoo, P. Thakur, R. Sharma, S. Bawari, R. Podila, T. N. Narayanan, *Phys. Chem. Chem. Phys.* **2019**, *21*, 3942.
[65] C. Wu, A. M. Soomro, F. Sun, H. Wang, Y. Huang, J. Wu, C. Liu, X. Yang, N. Gao, X. Chen, J. Kang, *Sci. Rep.* **2016**, *6*, 34766.
[66] D. Lee, S. H. Song, *RSC Adv.* **2017**, *7*, 7831.
[67] T. Shen, S. Liu, W. Yan, J. Wang, *J. Mater. Sci.* **2019**, *54*, 8852.
[68] K. K. Kim, S. M. Kim, Y. H. Lee, *J. Korean Phys. Soc.* **2014**, *64*, 1605.
[69] O. Hod, *J. Chem. Theory Comput.* **2012**, *8*, 1360.
[70] A. G. Kelly, T. Hallam, C. Backes, A. Harvey, A. S. Esmaeily, I. Godwin, J. Coelho, V. Nicolosi, J. Lauth, A. Kulkarni, S. Kinge, *Science* **2017**, *356*, 69.
[71] C. Backes, R. J. Smith, N. McEvoy, N. C. Berner, D. McCloskey, H. C. Nerl, A. O'Neill, P. J. King, T. Higgins, D. Hanlon, N. Scheuschner, *Nat. Commun.* **2014**, *5*, 4576.
[72] R. Kumar, S. K. Nayak, S. Sahoo, B. P. Panda, S. Mohanty, S. K. Nayak, *J. Mater. Sci.: Mater. Electron.* **2018**, *29*, 16932.
[73] Y. Cao, J. Zhang, D. Zhang, Y. Lv, J. Li, Y. Xu, K. He, G. Chen, C. Yuan, B. Zeng, L. Dai, *J. Mater. Sci.* **2020**, *55*, 11325.
[74] A. Pettignano, A. Charlot, E. Fleury, *Polymers* **2019**, *11*, 1227.
[75] S. S. Kang, in 2012 7th Int. Conf. Integr. Power Electron. Syst. (CIPS), IEEE, Nuremberg, Germany, March **2012**.
[76] D. Zhao, X. Qian, X. Gu, S. A. Jajja, R. Yang, *J. Electron. Packag.* **2016**, *138*, 040802.
[77] R. Li Voti, G. Leahu, E. Petronijevic, A. Belardini, T. Cesca, C. Scian, G. Mattei, C. Sibilia, *Appl. Sci.* **2022**, *12*, 1109.
[78] A. Hussanan, N. T. Trung, *J. Adv. Res. Fluid Mech. Therm. Sci.* **2019**, *56*, 248.
[79] S. Svetlov, N. Levina, A. Pivovarov, *Chem. Pet. Eng.* **2019**, *54*, 723.
[80] I. Y. Forero-Sandoval, F. Cervantes-Alvarez, J. A. Ramirez-Rincon, J. D. Macias, N. W. Pech-May, J. Ordonez-Miranda, J. J. Alvarado-Gil, *Appl. Compos. Mater.* **2021**, *28*, 447.
[81] S. Zhou, T. Xu, L. Jin, N. Song, P. Ding, *Compos. Sci. Technol.* **2022**, *219*, 109259.
[82] J. Wie, J. Kim, *Polymers* **2020**, *12*, 2553.
[83] C. Lin, D. Chung, *J. Electron. Mater.* **2009**, *38*, 2069.
[84] C. Lin, T. A. Howe, D. Chung, *J. Electron. Mater.* **2007**, *36*, 659.
[85] A. Yazdan, J. Wang, C. W. Nan, L. Li, *J. Electron. Mater.* **2020**, *49*, 2100.
[86] Eletrolube. TCOR Thermally Conductive RTV (Oxime) **2013**, p. 2.
[87] Vakefield-vette. Thermal Compounds, Adhesives And Interface Materials **2007**, p. 5.

© 2024 The Author(s). Advanced Functional Materials published by Wiley-VCH GmbH

16163028, 0, Downloaded from https://onlinelibrary.wiley.com/doi/10.1002/adfm.202405235 by Cochraneltalia, Wiley Online Library on [14/07/2024]. See the Terms and Conditions (https://onlinelibrary.wiley.com/terms-and-conditions) on Wiley Online Library for rules of use; OA articles are governed by the applicable Creative Commons License